

# Suzaku Observations of the North Polar Spur: Evidence for Nitrogen Enhancement

Eric D. MILLER,<sup>1</sup> Hiroshi TSUNEMI,<sup>2</sup> Mark W. BAUTZ,<sup>1</sup> Dan MCCAMMON,<sup>3</sup> Ryuichi FUJIMOTO,<sup>4</sup>  
John P. HUGHES,<sup>5</sup> Satoru KATSUDA,<sup>2</sup> Motohide KOKUBUN,<sup>6</sup> Kazuhisa MITSUDA,<sup>4</sup> F. Scott PORTER,<sup>7</sup>  
Yoh TAKEI,<sup>4,8</sup> Yohko TSUBOI,<sup>9</sup> Noriko Y. YAMASAKI<sup>4</sup>

<sup>1</sup>*Kavli Institute for Astrophysics and Space Research, Massachusetts Institute of Technology, Cambridge, MA 02139, USA*

<sup>2</sup>*Department of Earth and Space Science, Osaka University, Toyonaka, Osaka 560-0043*

<sup>3</sup>*Department of Physics, University of Wisconsin, Madison, WI 53706, USA*

<sup>4</sup>*Institute of Space and Astronautical Science (ISAS), Japan Aerospace Exploration Agency (JAXA),  
3-1-1 Yoshinodai, Sagami-hara, Kanagawa 229-8510*

<sup>5</sup>*Department of Physics and Astronomy, Rutgers University, Piscataway, NJ 08854-8019, USA*

<sup>6</sup>*Department of Physics, University of Tokyo, 7-3-1 Hongo, Bunkyo-ku, Tokyo 113-0033*

<sup>7</sup>*NASA/Goddard Space Flight Center, Greenbelt, MD 20771, USA*

<sup>8</sup>*Netherlands Institute for Space Research (SRON), Sorbonnelaan 2, 3584 CA Utrecht, the Netherlands*

<sup>9</sup>*Department of Physics, Chuo University, 1-13-27 Kasuga, Bunkyo-ku, Tokyo 112-8551  
milleric@mit.edu*

(Received 30 May 2007; accepted 28 August 2007)

## Abstract

We present observations of the North Polar Spur (NPS) using the X-ray Imaging Spectrometer (XIS) aboard the *Suzaku* X-ray satellite. The NPS is a large region of enhanced soft X-ray and radio emission projected above the plane of the Galaxy, likely produced by a series of supernovae and stellar winds from the nearby Sco-Cen OB association. The exceptional sensitivity and spectral resolution of the XIS below 1 keV allow unprecedented probing of low-energy spectral lines, including C VI (0.37 keV) and N VII (0.50 keV), and we have detected highly-ionized nitrogen toward the NPS for the first time. For this single pointing toward the brightest 3/4 keV emission ( $l = 26.8^\circ$ ,  $b = +22.0^\circ$ ), the best-fit NPS emission model implies a hot ( $kT \approx 0.3$  keV), collisional ionization equilibrium (CIE) plasma with depleted C, O, Ne, Mg, and Fe abundances of less than 0.5 solar, but an enhanced N abundance, with  $N/O = (4.0^{+0.4}_{-0.5})$  times solar. The temperature and total thermal energy of the gas suggest heating by one or more supernovae, while the enhanced nitrogen abundance is best explained by enrichment from stellar material that has been processed by the CNO cycle. Due to the time required to develop AGB stars, we conclude that this N/O enhancement cannot be caused by the Sco-Cen OB association, but may result from a previous enrichment episode in the solar neighborhood.

**Key words:** ISM: abundances — ISM: structure — ISM: supernova remnants — ISM: individual (North Polar Spur) — X-rays: ISM

## 1. Introduction

The North Polar Spur (NPS) is a region of enhanced soft X-ray and radio emission projected above the plane of the Galaxy, associated with the bright radio continuum source called Loop I. Early studies suggested that Loop I is an old, nearby supernova remnant (SNR), with a shell of non-thermal, polarized radio continuum emission surrounded by a shell of slowly-expanding neutral gas (Berkhuijsen 1971; Berkhuijsen et al. 1971; Sofue et al. 1974; Heiles et al. 1980). Early rocket-based X-ray observations supported the SNR view, with detection of emission that could be explained by diffuse shock-heated plasma (Bunner et al. 1972; Cruddace et al. 1976; Iwan 1980; Schnopper et al. 1982; Rocchia et al. 1984). Additional work by de Geus (1992) showed that the combined stellar winds and supernovae from the centrally-located Scorpius-Centaurus OB association are sufficient

to sweep out shells in the ISM, forming the loop-like structures we see.

The *ROSAT* mission provided an unprecedented X-ray view of the NPS, which shows up clearly in the 3/4 keV all-sky map (Snowden et al. 1997). Using these data, Egger (1995) and Egger & Aschenbach (1995) also suggest that Loop I was produced by the continuous effects of supernovae and combined stellar winds from the Sco-Cen association. They conclude that the bright NPS emission arises from the most recent supernova shock wave heating the outer shell of the superbubble, at a distance of about 100 pc from the Sun. Notably, the authors propose an interaction between the Loop I superbubble and the Local Hot Bubble, citing detection of X-ray shadowing from a dense ring of H I at this interface.

A different scenario has been argued in a series of papers by Sofue (1977; 1984; 1994; 2000; 2003) and recently by Bland-Hawthorn & Cohen (2003). Under this model,

the NPS is the remnant of a starburst or explosion near the Galactic center 15 Myr ago and is at a distance of several kpc. This scenario is based largely on morphological arguments, however, and it is contradicted by other observations. For example, Mathewson & Ford (1970) detect an interstellar polarization feature at a distance of about 100 pc which clearly follows much of the northern and eastern parts of Loop I, including the NPS, with the expected polarization orientation. In addition, the H I features seen nearby appear to be due to an interaction of Loop I with the Local Bubble, as previously described (Egger & Aschenbach 1995). These results strongly favor the local NPS model, although the Galactic center model cannot yet be ruled out.

Our understanding of the origin of the NPS hinges on the plasma conditions, including temperature and metal abundance, which can be constrained by current X-ray instrumentation. However, X-ray observations along this line of sight are complicated by the contribution of various emission sources comprising the soft X-ray background (SXRb). The Local Hot Bubble (LHB; Snowden et al. 1990 and references therein), Galactic halo, and additional diffuse Galactic material produce thermal emission below 2 keV, consistent with 0.1–0.2 keV plasma, and dominated by low-energy emission lines. Contributions from unresolved Galactic and extragalactic point sources produce continuum emission across a broad energy band. These emission components are affected by differing amounts of intervening absorption.

Recent *XMM-Newton*/EPIC-MOS observations of three NPS pointings at low latitude offer some insight, modeling the various line-of-sight emission components and identifying a  $kT \approx 0.25$  keV plasma with bright emission lines and metal abundances of about 0.5 solar (Willingale et al. 2003). This high-temperature emission is associated with the enhanced NPS feature seen in the *ROSAT* maps, and it supports the view that the emission arises from re-heating of a superbubble shell.

The relative chemical abundances and the plasma conditions within the NPS hold the key to its formation. With *Suzaku* we are able to probe the low-energy emission lines of C VI (0.37 keV), N VI (0.43 keV), and N VII (0.50 keV) in this region for the first time. Thanks to an unprecedented combination of effective area and spectral resolution from a CCD-based instrument, the XIS (Koyama et al. 2007) has produced new results on a range of soft X-ray sources (Miyata et al. 2007; Fujimoto et al. 2007; Smith et al. 2007; Hamaguchi et al. 2007). Here we present *Suzaku*/XIS observations of the NPS in an effort to further constrain the temperature, abundance, and structure of the emitting material.

Throughout this paper, errors associated with values in the text or tables are at 90% confidence for a single parameter, unless otherwise noted. Error bars shown in figures are  $1\text{-}\sigma$ .

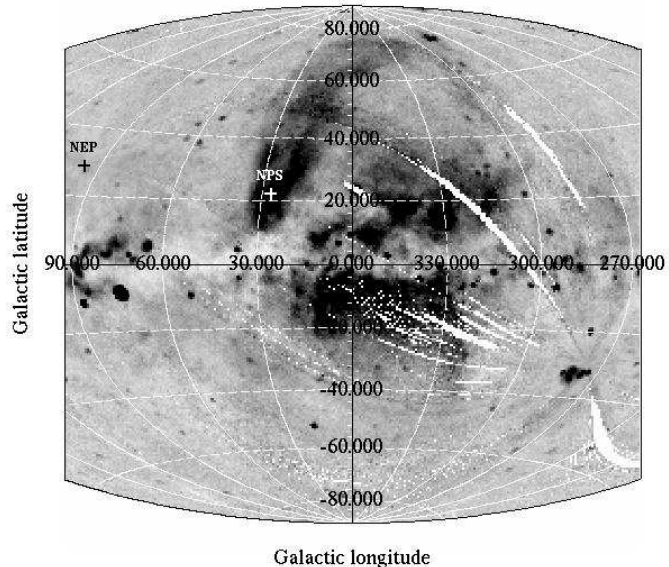


**Fig. 1.** *ROSAT* 3/4 keV map toward the Galactic center, shown in inverse grayscale (Snowden et al. 1997). The location of our *Suzaku* NPS pointing is indicated by the white cross. The location of the off-source NEP observation is shown by a black cross.

## 2. Observations and Data Reduction

The NPS was observed by the *Suzaku*/XIS during Science Working Group (SWG) time on 3–4 October 2005 (ObsID 100038010), for a total integration time of 46.1 ksec. The pointing was chosen from the peak of the NPS emission seen in the 3/4 keV *ROSAT* all-sky survey map (Snowden et al. 1997), toward  $l = 26.8^\circ$ ,  $b = +22.0^\circ$  (see Figure 1). The observing parameters are listed in Table 1.

### 2.1. Initial Data Preparation

The data were processed with rev0.7 of the XIS pipeline processing software, producing a set of cleaned event lists with hot pixels removed and including only ASCA grades<sup>1</sup> 0,2,3,4,6. The recommended filtering criteria<sup>2</sup> were used to remove SAA transits and times of low geomagnetic cut-off rigidity (COR), eliminating data with  $COR < 6$  GV. In addition, all data taken within  $20^\circ$  of the sun-lit Earth limb or  $10^\circ$  of the dark Earth limb were excised to reduce contamination from scattered solar X-ray flux. Times of telemetry saturation were removed as well.

Analysis of the light curves revealed some times of high count rate for two of the detectors, XIS0 and XIS1. The high count rate in XIS0 lasted a single orbit and was due to a high CCD temperature, the result of a temporary thermal control system anomaly. Housekeeping and count rate data from the previous and subsequent orbits were normal, so only data during the affected orbit were excised,

<sup>1</sup> See *The ASCA Data Reduction Guide* (<http://heasarc.gsfc.nasa.gov/docs/asca/abc/abc.html>).

<sup>2</sup> See *The Suzaku Data Reduction Guide* (<http://heasarc.gsfc.nasa.gov/docs/suzaku/analysis/abc/>).

**Table 1.** Observing Parameters

Target	North Polar Spur	North Ecliptic Pole <sup>a</sup>
Date	3–4 Oct 2005	2 Sep 2005
(ObsID)	(100038010)	(100018010)
		12 Feb 2006
		(500026010)
$\alpha$	17 <sup>h</sup> 22 <sup>m</sup> 21 <sup>s</sup> .0	18 <sup>h</sup> 11 <sup>m</sup> 12 <sup>s</sup> .0
$\delta$	+04°45′24″	+66°00′00″
$l$	26.°84	95.°77
$b$	+21.°96	+28.°67
$N_{\text{H}}$ (cm <sup>-2</sup> ) <sup>b</sup>	$5.63 \times 10^{20}$	$4.3 \times 10^{20}$
$t_{\text{exp,flt}}$ (ksec) <sup>c</sup>		
XIS0	35.7	136.7
XIS1	39.9	142.3
XIS2	38.4	136.4
XIS3	38.7	137.9

<sup>a</sup> This dataset was used as an off-source background.<sup>b</sup> Dickey & Lockman (1990)<sup>c</sup> Effective exposure time of filtered datasets.

eliminating 4.2 ksec of exposure time for XIS0. The high count rate in the back-illuminated (BI) chip XIS1 arises from variations in the particle background as a result of varying geomagnetic shielding (e.g., Snowden 1998; Tawa et al. 2007). Rejection of particle events is less effective for the BI sensor than the front-illuminated (FI) sensors, and this produces a higher measured background. Filtering based on the cut-off rigidity can reduce the background, but at a cost of reduced exposure time. Further considerations of the particle background are addressed in Section 2.3.3. The combined filtering removed 22% of XIS0 data, 13% of XIS1 data, and 16% of XIS2 and XIS3 data. The effective exposure times are shown in Table 1.

As described in Section 3.2.1, we have used additional *Suzaku* observations of the North Ecliptic Pole (NEP) as a background field. These observations were carried out on 2 September 2005 (ObsID 100018010) and 12 February 2006 (ObsID 500026010), also during *Suzaku* SWG time, and have been presented by Fujimoto et al. (2007). The NEP data were processed in the same manner as the NPS data, using rev0.7 software and identical filtering criteria. The observations are summarized in Table 1.

Visual inspection of the binned broad-band image of the NPS field reveals a number of likely point sources, including a bright source falling near the center of the field (see Figure 2). To compromise between removing all the point source flux and maximizing the diffuse emission coverage, we used a smaller-than-normal masking/extraction region for the bright central source (2.7′ radius rather than the nominal 4.3′, 6 mm aperture for which the standard ARFs have been constructed). Four likely additional point sources were masked by hand. See Section 3.1 for an analysis of these sources.

Spectra were extracted for each point source and for the portion of the NPS field of view excluding these sources. This latter “point source exclusion” extraction was used as both the diffuse emission spectrum and the background spectrum for the point sources. The off-source background

spectrum from the NEP was extracted from an identical region projected in detector coordinates.

## 2.2. Contamination and Calibration Corrections

Early in the *Suzaku* mission, it was discovered that the low-energy effective area of each XIS instrument was deteriorating, likely due to a build-up of contamination on the optical blocking filter of each sensor (Koyama et al. 2007). Subsequent observations of calibration sources have shown that the contamination is composed primarily of carbon with small amounts of oxygen, and that the rate of deposition appears to be decreasing. In addition, the inferred thickness varies from sensor to sensor, and the amount of contamination is non-uniform across each sensor, with larger optical depth in the center (Koyama et al. 2007). The effective area of the XIS at low energies is therefore dependent on chip location, energy, and time.

To account for the contamination, we have used the empirical model developed by the XIS calibration team. This relies on regular (approximately monthly) observations of point source calibration targets as well as monthly accumulations of diffuse, bright Earth limb data. We used the *Suzaku* xissimarfgen tool (version 2006-10-26) to construct the ancillary response functions (ARFs) for each spectral extraction region discussed in this work. This software corrects for the off-axis vignetting as well as the spatial-, time- and energy-dependence of the contamination, using the most reliable evolutionary model as of 2006-10-16, and assuming a surface contaminant consisting solely of carbon and oxygen in the number ratio  $N_{\text{C}}/N_{\text{O}} = 6$  (Ishisaki et al. 2007).

We note that the contamination was discovered a month after the NPS observations were completed, and the inferred contaminant thickness was changing quite rapidly at that point in the mission (see Figure 14 of Koyama et al. 2007; the NPS was observed 52 days after the XIS doors opened on 2005 August 13). The contamination was relatively small, with central contaminant transmis-



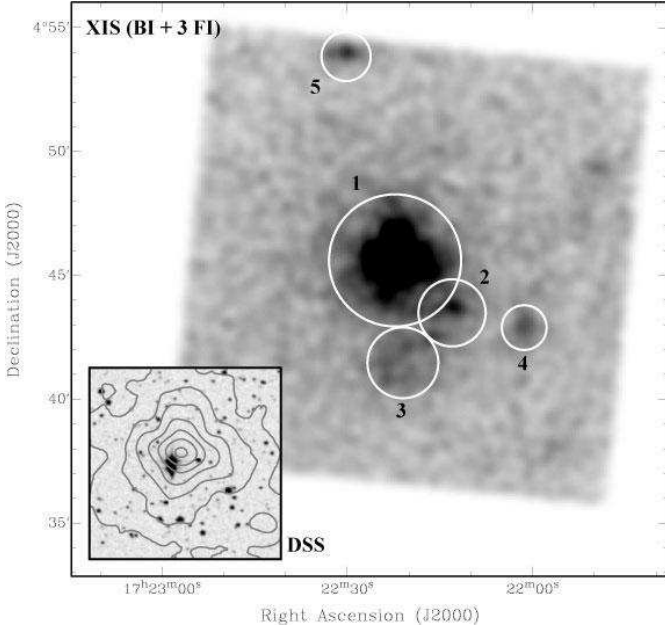


**Fig. 2.** Combined 0.3–5.0 keV image of the XIS field of view, shown in inverse grayscale. Likely point sources are identified by white circles and are discussed further in the text. The optical Digitized Sky Survey image of the XIS field of view is shown as an inset, with the X-ray image overplotted in contour. The bright central X-ray point source (1RXS J172223.9+044515) falls very close to a bright optical double star.

sion at 0.5 keV (near the N VII line) ranging from 88% (for the BI chip, XIS1) to 68% (for XIS3, the worst FI case). Nevertheless, uncertainties in the contamination are a source of systematic error in the broadband spectral modeling presented here.

The gain and spectral resolution of each CCD change on-orbit due to radiation-induced decreases in the charge transfer efficiency. To account for this, we have constructed redistribution matrix functions (RMFs) using the *Suzaku* xisrmfgen tool, version 2006-10-26. These RMFs were used in the spectral fitting discussed throughout this paper.

### 2.3. Background Correction

Spectral analysis of a diffuse source hinges on proper treatment of the background, as parameters such as temperature can be affected by erroneous modeling. X-ray instruments in flight detect background counts from a number of sources, and here we treat each one in some detail.

#### 2.3.1. Scattered Solar X-rays

X-rays from the sun scatter off the outer parts of the Earth’s atmosphere, producing soft, field-filling emission which is indistinguishable from a diffuse cosmic source (for a review see Snowden & Freyberg 1993). Two processes dominate: Thomson scattering off of molecules and atoms, which mimics the line-rich solar spectrum at low energies; and fluorescence scattering, which produces emission lines from the primary atmospheric constituents, atomic and

molecular nitrogen and oxygen. This contamination, especially from O K $\alpha$  fluorescence near 0.53 keV, complicates spectral modeling near the energies we expect to see carbon and nitrogen emission from the NPS and could produce false detections of these lines.

Since the intensity of scattered solar radiation depends on the column density of the residual sun-lit atmosphere, the count rate is modulated over the orbit. Limits on solar contamination can be inferred from measuring the soft X-ray count rate as a function of the sun-lit column density along the line of sight. Using the NRLMSISE-00 empirical model of the atmosphere (Picone et al. 2002), we have estimated the total sun-lit O<sub>2</sub> plus O column along the telescope line of sight during the NPS observation. This is plotted in Figure 3 against the count rate in the XIS1 0.4–1 keV band, in which we expect oxygen fluorescence to produce the majority of flux. The top panel shows the count rate with no filtering based on Earth angle, and the rate clearly increases when the total oxygen column exceeds  $10^{14}$  cm<sup>-2</sup>. These high column density observations are eliminated with the standard Earth angle filtering, as shown in the bottom panel of Figure 3.

To estimate the magnitude of solar X-ray contamination, we follow the method used by Smith et al. (2007) in their *Suzaku* shadowing observations toward the MBM 12 molecular cloud. We fit a linear function to the top panel of Figure 3 for  $N(\text{O} + \text{O}_2) = 0\text{--}10^{17}$  cm<sup>-2</sup>, obtaining a best fit count rate of  $(0.404 \pm 0.003) + (9.2 \pm 0.1) \times 10^{-16} N(\text{O} + \text{O}_2)$  cts s<sup>-1</sup> (1- $\sigma$  errors). Here the slope provides an estimate of the scattered solar X-ray flux, while the intercept represents the count rate from all other sources, including cosmic X-ray emission and the particle background. For comparison, the slope measured here is about 8 times larger than that for the MBM 12 observations (Smith et al. 2007), indicating a larger contamination from scattered solar X-ray flux at a given sun-lit column density.

While the filtering on Earth angle eliminates column densities greater than  $5 \times 10^{12}$  cm<sup>-2</sup>, about 50% of the observing time occurs at column densities between  $5 \times 10^{11}$ – $5 \times 10^{12}$  cm<sup>-2</sup>, where we expect solar contamination of a few percent. We integrate the linear slope over the good time intervals for the observation, estimating a scattered solar count rate of 0.0012 cts s<sup>-1</sup> in the 0.4–1 keV energy range. This is equivalent to a flux of 0.02 cts s<sup>-1</sup> keV<sup>-1</sup> at 0.53 keV if all the emission is in the O K $\alpha$  line, assuming an instrumental line width of 70 eV FWHM. As discussed in Section 3.2.2, this amounts to a few percent of the count rate in the N VII and O VII line region.

#### 2.3.2. Solar Wind Charge Exchange

Heavy ions in the solar wind undergo charge exchange (SWCX) with neutral atoms in the Earth’s geocorona and in the interplanetary medium. The resulting excited atoms release X-ray line emission which is generally field-filling and indistinguishable from the more distant plasma emission under study. The solar wind heavy ion flux determines the X-ray line strengths, and thus variations in the solar wind produce variations in the contaminating flux on timescales of seconds (for geocoronal SWCX) to

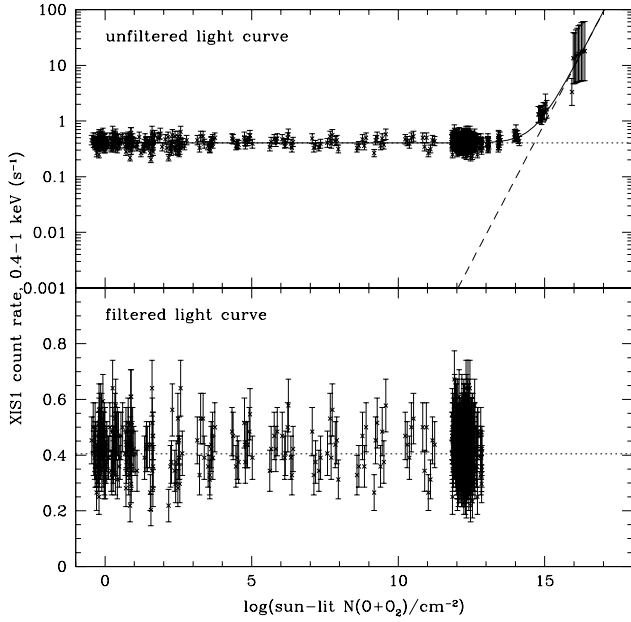


**Fig. 3.** Count rate for XIS1 as a function of sun-lit oxygen column density, in the 0.4–1 keV range. The oxygen column density includes contributions from atomic and molecular states. The top panel includes all X-ray events without filtering for Earth angle, and scattered solar flux clearly contaminates above  $N(\text{O} + \text{O}_2) \approx 10^{14} \text{ cm}^{-2}$ . The solid line shows the best fit linear function described in the text, with intercept due to the source flux (dotted line) and slope due to the scattered solar flux (dashed line). The bottom panel shows the count rate on a linear scale, with data filtered as described in Section 2.1. All data used in this analysis were acquired with sun-lit column densities below  $10^{13} \text{ cm}^{-2}$ , and by extrapolating the linear function, we expect scattered solar flux to contribute a few percent of the count rate in this energy range.

days or longer (for interplanetary SWCX; e.g., Cravens 2000).

Mitigation strategies exist, as described by Fujimoto et al. (2007), who detect a short-term charge exchange enhancement in a long *Suzaku* observation toward the NEP. We follow the lead of these authors and Smith et al. (2007), and note the following. First, the soft X-ray count rate shows little variability with time, implying no charge exchange variability on timescales less than 85 ksec (see Figure 4, top panel). Second, we have analyzed public data from the *Advanced Composition Explorer* (ACE) satellite (Stone et al. 1998), which measures solar wind properties, taken during our observation (Raines et al. 2005). The flux of protons,  $\text{C}^{+6}$  ions, and  $\text{O}^{+7}$  ions are shown in Figure 4, corrected for the travel time from ACE to the Earth. The proton flux varies by less than a factor of 1.4 during the *Suzaku* observation, and it is about half the value seen during the NEP flare, or nearly the quiescent value during that observation (Fujimoto et al. 2007). The ion fluxes are at least as low as the NEP quiescent times. We conclude that geocoronal SWCX is unlikely to contaminate our data, but we cannot at this point con-

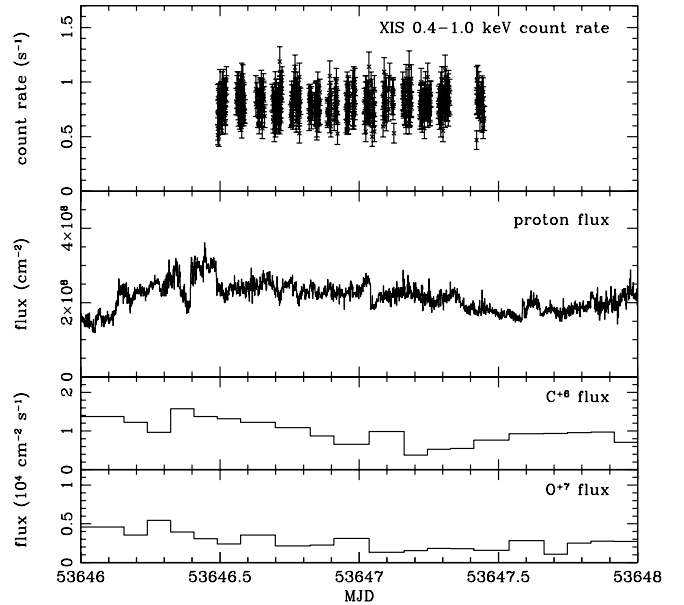


**Fig. 4.** The top panel shows the combined 0.4–1.0 keV light curve for all four XIS sensors. The lower three panels show data collected by the ACE satellite, corrected for travel time to the Earth, and used to estimate the effects of geocoronal SWCX. The second panel shows the proton flux, the third panel shows the  $\text{C}^{+6}$  ion flux, and the bottom panel shows the  $\text{O}^{+7}$  ion flux. The time range was chosen to look for solar wind enhancements of longer duration than our observations. There is no significant flare in the light curve, and no apparent solar wind flux enhancements, so we conclude that geocoronal SWCX is unlikely to contaminate our observations.

strain the effects of SWCX in the interplanetary medium.

Since we use the NEP observations as an off-source background, we have screened these data to remove the SWCX flare (Fujimoto et al. 2007). There is no evidence for additional SWCX contamination in these observations. The final effective exposure time for the NEP data used as background is shown in Table 1.

### 2.3.3. Particle Background

All four sensors show count rate variations that are well-correlated with the change in geomagnetic cut-off rigidity as the satellite orbits. These variations are similar to what is seen in observations dominated by the particle background (Tawa et al. 2007). A larger COR prevents energetic particles from penetrating to the orbit of the satellite, reducing the background count rate. This is especially evident in the BI sensor, XIS1. Due to its smaller depletion depth, the particle rejection efficiency of XIS1 is lower than that of the FI chips, and it has a larger particle background between 5–12 keV and a more noticeable count rate variation. To reduce the background, we experimented with changing the minimum COR value and analyzing the resultant light curves and spectra. The default constraint of  $\text{COR} < 6 \text{ GV}$  was found to be the best compromise between minimum particle background and maximum exposure time, so no additional filtering was performed.

Since the NPS and X-ray background emission sources are field-filling, we must use non-contemporaneous observations to estimate the particle background. We used 800 ksec of data accumulated during observations of the dark (night) Earth between 04 September 2005 and 21 May 2006 (Tawa et al. 2007). These data were processed with rev0.7 of the pipeline software, filtered for telemetry saturation and extracted using the same detector regions as the science data to eliminate any spatial dependence. The background event rate is well-correlated with the COR, as expected. Since the NPS observations were taken at a different time, the COR distribution and thus the integrated count rate will be different for the accumulated night Earth data compared to the true particle background during the science observations. To correct for this, we have constructed a COR-weighted background spectrum that comprises the same COR time fractions as the NPS observations. Similar COR weighting was performed on the NEP data.

#### 2.3.4. Cosmic Background

Galactic and extragalactic emission contributes to the background along the line of sight. Since it is difficult to separate these sources from the extended NPS emission under study, we account for them in the spectral modeling described in Section 3.2.1.

### 3. Analysis

#### 3.1. Point-Like Sources

The XIS field of view contains several point sources, including a bright source located near the pointing center. Two of these sources are found in the *ROSAT* All-Sky Bright Source Catalog (Voges et al. 1999; sources 1 and 5 in Figure 2), although they have no classification. The other sources are not associated with any known X-ray source.

Source 1 is identified as 1RXS J172223.9+044515, a known X-ray source within  $30''$  of the XIS peak flux (and within the pointing error circle of rev0.7 XIS data). A search in other wavebands produces a known double star near this location, HD 157310 ( $B=10.1, V=9.8$ ) and BD+04 3405B ( $V=10.8$ ; see Figure 2). The fainter star is within  $6''$  of the cataloged position for the RXS source.

The X-ray spectrum, shown in Figure 5, was fitted with a number of models. The background was provided by the full field of view, excluding the point sources. Absorbed single-emission-component models (blackbody, thin thermal plasma, or power-law) are ruled out as poor fits. Two-component models produce better results, with similar fits coming from an absorbed thermal+power-law model and an absorbed thermal+thermal model ( $\chi_r^2 = 1.3$ – $1.5$ ), using the APEC model (Smith et al. 2001) for the optically thin thermal emission component. The model parameters are listed in Table 2; both models require a  $kT \approx 0.75$  keV thermal plasma, assuming solar abundances. The double thermal model requires little line-of-sight absorption, while the thermal+power-law model requires a solar-abundance absorbing column in excess of  $4.7 \times 10^{20} \text{ cm}^{-2}$ , which is about 80% of the expected Galactic value along

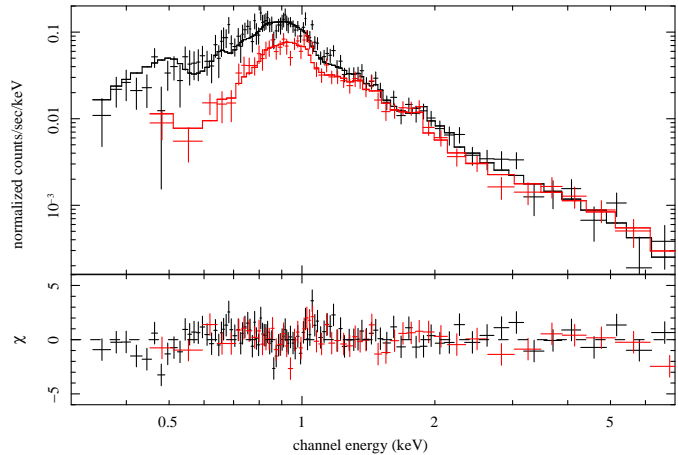


**Fig. 5.** Spectra of the bright point source 1RXS J172223.9+044515 (Source 1 in the text). Black shows the BI spectrum and red shows the averaged FI spectrum. Each is overplotted with the best-fit, APEC+power-law model. The lower panel shows the residuals.

**Table 2.** Model Parameters for 1RXS J172223.9+044515

	Model 1 <sup>a</sup>	Model 2 <sup>b</sup>
$kT_1$ (keV)	$0.75 \pm 0.02$	$0.75 \pm 0.02$
$kT_2$ (keV)	$3.1 \pm 0.3$	...
$\Gamma$	...	$2.3 \pm 0.1$
$N_H$ ( $10^{20} \text{ cm}^{-2}$ )	$< 0.5$	$> 4.7$
$\chi^2_\nu$ (dof)	1.04 (488)	1.02 (488)

<sup>a</sup> Absorbed, two-APEC model.

<sup>b</sup> Absorbed, APEC + power law model.

this line of sight. The 0.5–5 keV flux of the source is  $(5.8 \pm 0.2) \times 10^{-13} \text{ erg cm}^{-2} \text{ s}^{-1}$  ( $1\text{-}\sigma$  errors).

It is likely this X-ray source is associated with one of the two bright stars along this line of sight. The brighter star was originally classified as a G5 spectral type (Cannon & Pickering 1918), although later analysis classified it as A7II/III (Houk & Swift 2000). The fainter star has no published MK type. From simple spectral parallax, and ignoring extinction, the bright star would be about 88 pc distant if a G5 dwarf and 555 pc distant if an A7III. The unabsorbed 0.5–5 keV luminosities would be  $L_X(88 \text{ pc}) = 5.4\text{--}6.3 \times 10^{29} \text{ erg s}^{-1}$  and  $L_X(555 \text{ pc}) = 2.2\text{--}2.5 \times 10^{31} \text{ erg s}^{-1}$ , depending on the true absorbing column.

To search for variability, we produced a background-subtracted light curve and power spectrum from all four XIS sensors over the 0.5–5 keV band. These are shown in Figure 6. No variability is seen at periods less than about 30 min, down to the time resolution of 8 sec. A peak appears around 75 min, and peaks with less significance are present at longer periods. There is also a hint of flaring in the light curve. The low signal-to-noise of the source and background prevent a more quantitative timing analysis.

From the spectral model and likely optical counterpart, we tentatively classify this source as an RS CVn interacting binary. These systems produce strong thermal coronal emission, they are common soft X-ray sources in the

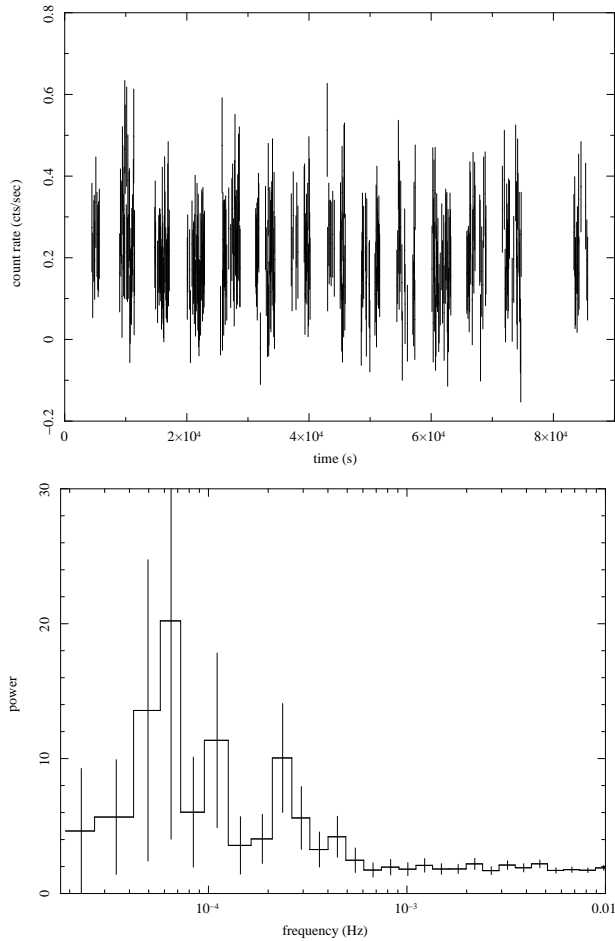


**Fig. 6.** Background-subtracted light curve (top) and power spectrum (bottom) for the bright central point source 1RXS J172223.9+044515. Data from all four sensors have been combined, spanning the 0.5–5.0 keV energy range. A hint of variability is seen, although the low signal-to-noise complicates analysis.

Galaxy, and the derived X-ray luminosities span the range expected for these objects (e.g., Drake et al. 1989). The light curve is also consistent with this conclusion, ruling out very large brightness fluctuations but allowing flaring of less than 50% or so over time scales less than the 85 ksec observation window. Note that the distance inferred would place the source beyond the near edge of the assumed NPS “bubble”, and the large absorbing column implied by the thermal+power-law model is consistent with results from fitting the diffuse soft X-ray emission (see Section 3.2.1). Further classification of this source would require detailed optical and UV spectroscopic analysis, which is beyond the scope of this paper.

Source 2 is projected 3' from the central source, and has no known X-ray counterpart within the expected pointing error circle. It lies 30'' from a known radio source, RC J1722+0442, which has been identified from broad-band optical spectroscopy as a  $z \approx 1$  radio galaxy (Verkhodanov et al. 2002). The extracted spectra for this source are of low S/N, and therefore we have not performed additional analysis. Sources 3 and 4 are very faint, although they

appear to be discrete emission. There are no counterparts for these objects in the literature. Source 5 is within 30'' of the *ROSAT* object 1RXS J172228.9+045402, although it falls at the very edge of the field of view, making analysis difficult.

### 3.2. Diffuse Emission

#### 3.2.1. Spectral Modeling

The line of sight to the NPS probes a number of foreground and background sources which emit soft X-ray radiation. The degree of absorption expected in each component depends on the particular schematic model invoked, of which there are several in the literature (Iwan 1980; Davelaar et al. 1980; de Geus 1992; Egger & Aschenbach 1995; Willingale et al. 2003). The models invariably include an unabsorbed Local Hot Bubble plasma that extends 50–100 pc from the Sun, depending on the pointing direction. This is terminated by a dense H I sheet inferred from differential absorption in spectra of stars at known distance (Iwan 1980; Centurion & Vladilo 1991; Egger & Aschenbach 1995). This sheet encloses the Loop I (and NPS) bubble and has a column density of  $10^{20}$ – $10^{21}$  cm $^{-2}$ . The NPS bubble fills some portion of the Loop I bubble, beyond which lies the residual Galactic H I column, the Galactic halo plasma, and any extragalactic diffuse and unresolved point-source emission.

To allow direct comparison to the *XMM-Newton* data, we have adopted the spectral model components of Willingale et al. (2003), who observed three fields towards the NPS at slightly different Galactic latitudes with the EPIC-MOS. This model consists of an unabsorbed, solar-abundance Local Hot Bubble (LHB) with fixed  $kT = 0.1$  keV; a single-temperature, solar-abundance Galactic halo (GH) component with fixed  $kT = 0.1$  keV, subject to the full Galactic absorbing column; a broken power-law extragalactic background (EB) to account for unresolved point sources, with photon indices  $\Gamma(< 0.7 \text{ keV}) = 2.0$  and  $\Gamma(> 0.7 \text{ keV}) = 1.4$ , subject to the full Galactic absorbing column; and a thermal NPS component with freely-varying  $kT$ , abundances, and  $N_{\text{H}}$ . The LHB, GH, and EB components together form the X-ray background (XRB), and we allow only the normalizations of these components to vary. The shape of the EB power-law is identical to that used by Willingale et al. (2003), and it includes a steepening at softer energies to account for unresolved Type I AGN (e.g., Roberts & Warwick 2001; Bauer et al. 2004; De Luca & Molendi 2004). In the remainder of this paper, we refer to this set of spectral components as the “local background model”, since it accounts for the background directly along the NPS sightline.

The model fitting was performed on all four XIS spectra simultaneously using XSPEC v.12.3.1 (Arnaud 1996). The APEC model (Smith et al. 2001) was used for thin thermal plasma components (LHB, GH, and NPS), with freely-varying C, N, O, Ne, Mg, and Fe abundances for the NPS. We fixed the Galactic  $N_{\text{H}}$  absorbing column to  $5.63 \times 10^{20}$  cm $^{-2}$  (Dickey & Lockman 1990), using this as a maximum allowable value for the NPS component. We perform the fitting over the 0.4–3 keV energy range



for the FI detectors and 0.3–3 keV for the BI detector. While the XIS BI device has measurable sensitivity between 0.2–0.3 keV (the C-band), due to uncertainties in the XIS calibration and deficiencies in the APEC model (R. Smith, private communication) in this energy range, we have excluded it from our analysis. An accumulated, COR-weighted spectrum of the dark Earth was used to subtract the particle background, as described in Section 2.3.3.

As a check, we performed a model fit with an off-source pointing to characterize the background, using the two long SWG observations of the NEP (Fujimoto et al. 2007). While this pointing is  $62^\circ$  away from the NPS and at a very different Galactic longitude ( $96^\circ$  for the NEP vs.  $27^\circ$  for the NPS), it is at a similar Galactic latitude ( $29^\circ$  vs.  $22^\circ$ ; see Figure 1). As such, it provides a first-order removal of the X-ray background components (LHB, GH, EB) and the particle background (after correcting to a similar COR distribution; see Section 2.3.3). We note that the Galactic absorbing column is somewhat lower toward the NEP ( $4.3 \times 10^{20} \text{ cm}^{-2}$ ) than the NPS ( $5.6 \times 10^{20} \text{ cm}^{-2}$ ; Dickey & Lockman 1990), and we do not take this into account. The NEP spectrum is subtracted from the NPS spectrum during fitting, and we fit only a single absorbed APEC component representing the NPS plasma. The absorbing  $N_{\text{H}}$  is allowed to vary up to the maximum value of  $5.6 \times 10^{20} \text{ cm}^{-2}$ , and the plasma temperature, normalization, and C, N, O, Ne, Mg, and Fe abundances are also allowed to vary. In the remainder of the paper, we refer to this model as the “off-source background model”.

The best-fit parameters obtained with these two background models are presented in Table 3, and spectra overlaid with the models are shown in Figures 7 and 8. The formal fit is poor for both models, with  $\chi_r^2 = 1.21$ – $1.24$ . The residuals in Figures 7 and 8 suggest that much of the discrepancy could be from incorrect modeling of the line spread function in the instrument response, as there are marked residuals in the wings of strong emission lines. The XIS1 residuals are larger than those for FI spectra; in particular, there is an excess of flux compared with the predicted model near 0.54 eV in the XIS1 spectrum, on the low energy side of the O VII line. Also, the Fe XVII complex near 0.72 keV is brighter in the XIS1 spectrum than the model and FI spectra suggest. These differences are possibly due to errors in the early response calibration for the BI sensor. The general continuum shape and other emission line fluxes appear to be satisfactorily modeled for both the BI and FI spectra.

In the local background model, different line-of-sight components dominate the emission at different energies. This can be seen in Figure 9, which shows the BI (XIS1) spectrum along with individual additive spectral components. Strong emission lines from C, N, O, Fe, Ne and Mg are clearly seen, with the majority of these lines (and the majority of the flux below 1.5 keV) produced by the NPS component. Notable exceptions are the C VI, N VI and O VII lines, which are produced largely by the Galactic halo component. The N VII emission line at 0.50 keV is seen toward the NPS for the first time, and in our model

**Table 3.** Diffuse Emission Model Parameters

background model	local <sup>a</sup>	off-source <sup>b</sup>
extragalactic backgr.		
$N_{\text{H}}/N_{\text{H,tot}}^c$	1	...
$\Gamma_1$	2.0	...
$\Gamma_2$	1.4	...
$E_{\text{break}}$ (keV)	0.7	...
norm at 1 keV (ph/cm <sup>2</sup> /s/keV/sr)	$7.5 \pm 0.4$	...
Local Hot Bubble		
$N_{\text{H}}/N_{\text{H,tot}}^c$	0	...
$kT$ (keV)	0.1	...
abundance <sup>d</sup>	solar	...
EM (pc cm <sup>-6</sup> )	< 0.0029	...
Galactic halo		
$N_{\text{H}}/N_{\text{H,tot}}^c$	1	...
$kT$ (keV)	0.1	...
abundance <sup>d</sup>	solar	...
EM (pc cm <sup>-6</sup> )	$0.056^{+0.006}_{-0.007}$	...
North Polar Spur		
$N_{\text{H}}/N_{\text{H,tot}}^c$	>0.71	>0.97
$kT$ (keV)	$0.29^{+0.01}_{-0.01}$	$0.26^{+0.01}_{-0.01}$
$C^d$	< 0.06	< 0.07
$N^d$	$1.33^{+0.52}_{-0.38}$	$0.55^{+0.10}_{-0.09}$
$O^d$	$0.33^{+0.10}_{-0.07}$	$0.16^{+0.01}_{-0.01}$
$Ne^d$	$0.51^{+0.16}_{-0.12}$	$0.27^{+0.03}_{-0.03}$
$Mg^d$	$0.46^{+0.16}_{-0.12}$	$0.33^{+0.07}_{-0.06}$
$Fe^d$	$0.50^{+0.13}_{-0.09}$	$0.33^{+0.04}_{-0.03}$
EM (pc cm <sup>-6</sup> )	$0.089^{+0.031}_{-0.023}$	$0.18^{+0.01}_{-0.01}$
$\chi_r^2$ (dof)	1.24 (961)	1.21 (964)

<sup>a</sup> The “local” background model fits all emission components along the NPS line of sight simultaneously. Only a particle background produced from night Earth observations is subtracted.

<sup>b</sup> The “off-source” background model uses the NEP field to subtract the EB, LHB, GH, and particle background components during spectral fitting.

<sup>c</sup> The ratio of the absorbing column to the full Galactic column along this line of sight,  $5.63 \times 10^{20} \text{ cm}^{-2}$  (Dickey & Lockman 1990).

<sup>d</sup> Abundances are given in terms of the solar value, as tabulated by Anders & Grevesse (1989).

it is produced by the NPS plasma, since the other thermal components are too cool for this ionization state to occur under collisional ionization equilibrium (CIE) conditions.

The two background models yield similar best-fit NPS temperature ( $kT = 0.26$ – $0.29$  keV), remarkable given the very different methods of accounting for the SXRb. Both fits suggest low abundances (about 0.2–0.5 solar) for the NPS plasma, although the off-source background model produces values half as large as the local background model. (Note we use the solar abundance tables of Anders & Grevesse (1989) to facilitate comparison to previous studies.) This difference highlights a difficulty of constraining the abundance of optically thin thermal plasmas at temperatures of  $1$ – $3 \times 10^6$  K using X-ray data. At these temperatures, the spectrum is dominated by bright emission lines from metals, and the continuum produced



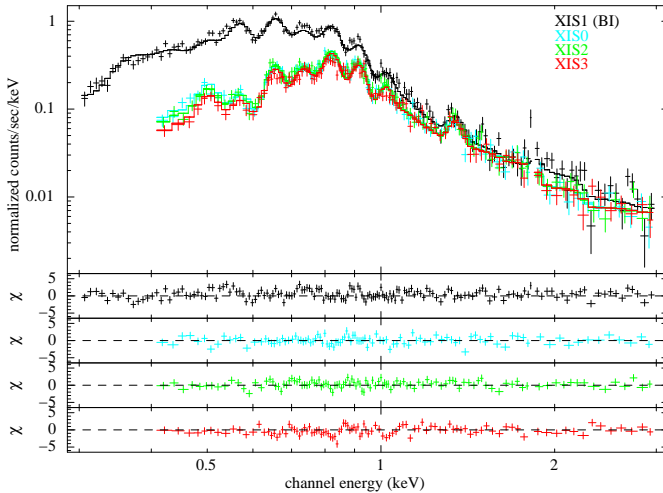


**Fig. 7.** *Suzaku*/XIS spectra of the NPS overlaid with the best-fit local background model. The particle background has been subtracted from the count rate spectra. Black is used for the BI spectrum (XIS1), red, green and cyan for the FI spectra. The lower panels show the fit residuals.

primarily by hydrogen and helium contributes only a few percent of the flux. Systematic uncertainties in the cosmic X-ray (AGN) and particle background limit the accuracy with which the continuum can be determined. At the low spectral resolution afforded by CCDs, uncertainties in the wings of the line redistribution function produce further errors at a flux level comparable to the continuum. The resulting poor constraints on the hydrogen number density yield poor constraints on metal abundance with respect to hydrogen, even though the metal emission line fluxes may be well-determined.

A more robust tracer of enrichment in low-temperature X-ray gas is the relative metal abundance. We have determined abundance ratios with respect to oxygen for each element in the NPS plasma. These are listed in Table 4 in terms of the solar abundance ratio from Anders & Grevesse (1989). Since best-fit absolute abundances are expected to be correlated and might not follow a normal distribution, we estimated abundance ratio confidence intervals with the Markov chain Monte Carlo (MCMC) simulator implemented in XSPEC v12.3.1, which employs the Metropolis-Hastings algorithm. We ran 20 parallel chains of 4000 steps each, throwing out the first 2000 steps and retaining the last 2000 steps for each chain. Random starting points were drawn from the multivariate normal approximation to the distribution produced in the original model fit. The temperature, individual metal abundances, and foreground absorption of the NPS plasma were free parameters for both background models. The normalization of the GH component was also allowed as a free parameter for the local background model. The Rubin-Gelman convergence parameter  $\sqrt{R}$  (Gelman & Rubin 1992) satisfied  $\sqrt{R} < 1.2$  for all parameters varied in the simulation, as required for convergence to an acceptably fair sample of the model parameter distribution. The results from all 20 chains were combined into

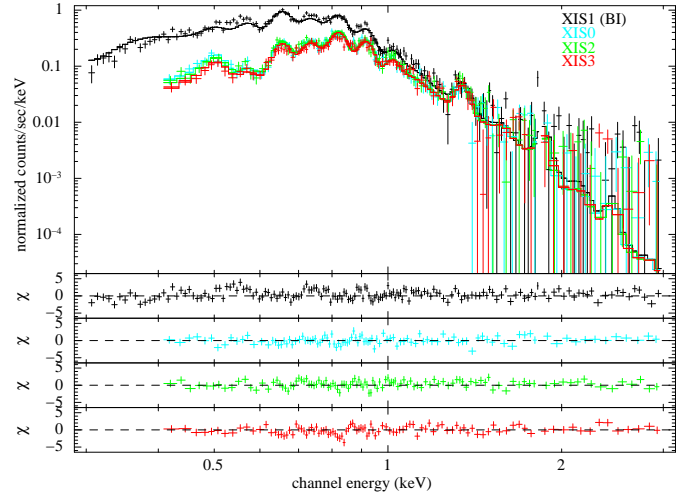


**Fig. 8.** *Suzaku*/XIS spectra of the NPS overlaid with the best-fit off-source background model. The particle background has been subtracted from the count rate spectra. Notations are identical to Figure 7.

**Table 4.** NPS Abundance Ratios<sup>a</sup>

	local background	off-source background
C/O	<0.17	<0.23
N/O	3.98 <sup>+0.43</sup> <sub>-0.45</sub>	3.41 <sup>+0.48</sup> <sub>-0.29</sub>
Ne/O	1.53 <sup>+0.13</sup> <sub>-0.11</sub>	1.68 <sup>+0.14</sup> <sub>-0.11</sub>
Mg/O	1.39 <sup>+0.29</sup> <sub>-0.24</sub>	2.05 <sup>+0.37</sup> <sub>-0.37</sub>
Fe/O	1.50 <sup>+0.14</sup> <sub>-0.12</sub>	2.07 <sup>+0.15</sup> <sub>-0.15</sub>

<sup>a</sup> Abundance ratios are shown in terms of the solar values from Anders & Grevesse (1989).

a single distribution, and central 90% confidence intervals were determined for each abundance ratio listed in Table 4. Compared to oxygen, the elements neon, magnesium, and iron are overabundant by factors of 1.4–2.1 in both the local and off-source models, while carbon is underabundant by a factor of about 5. Surprisingly, nitrogen is overabundant by a factor of  $4.0^{+0.4}_{-0.5}$  (local background) and  $3.4^{+0.5}_{-0.3}$  (off-source background) compared to oxygen.

### 3.2.2. Sources of Additional Emission

The constraints on the NPS nitrogen abundance come primarily from the N VII emission line. The excess of counts near 0.54 keV in the XIS1 spectrum bears consideration, since this is close to the energy of the N VII line. This excess is also seen in an XIS1 spectrum of the Carina Nebula (Hamaguchi et al. 2007), and the authors model it as a narrow Gaussian line at an energy of  $0.547 \pm 0.01$  keV. We do the same, adding a zero-width Gaussian component to the local background model and freezing all parameters at their best-fit values, allowing only the line energy and normalization to vary. Only the XIS1 data are included in the fit. The resultant line energy is  $0.54 \pm 0.02$  keV, in agreement with Hamaguchi et al. (2007). This energy is consistent with fluorescent scattering of solar X-rays from atmospheric oxygen, however the excess count rate of 2.0

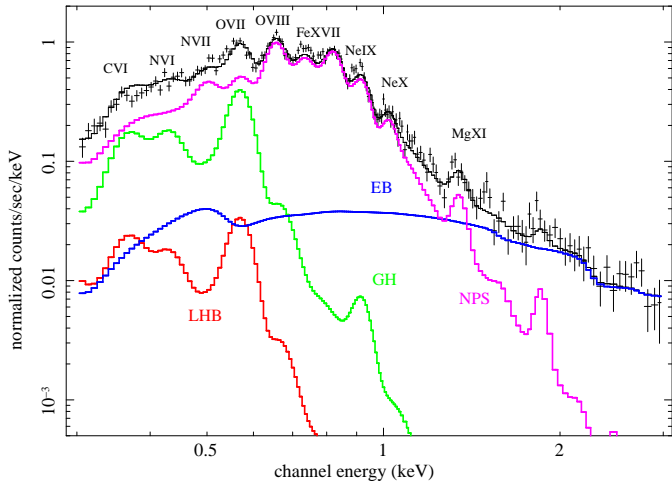


**Fig. 9.** *Suzaku*/XIS1 spectrum of the NPS, showing the additive emission components included in the local background model. Bright emission lines are marked with the species of the dominant transition responsible for the emission. The LHB component is plotted assuming the EM equals the 90% upper limit. The NPS plasma dominates the flux below 1.5 keV, producing the bright emission lines of N VII and O VIII, as well as lines from Fe, Ne and Mg. The Galactic halo component contributes to the C VI, N VI, and O VII lines. The N VII line at 0.50 keV can only be produced by the hotter NPS plasma in this model.

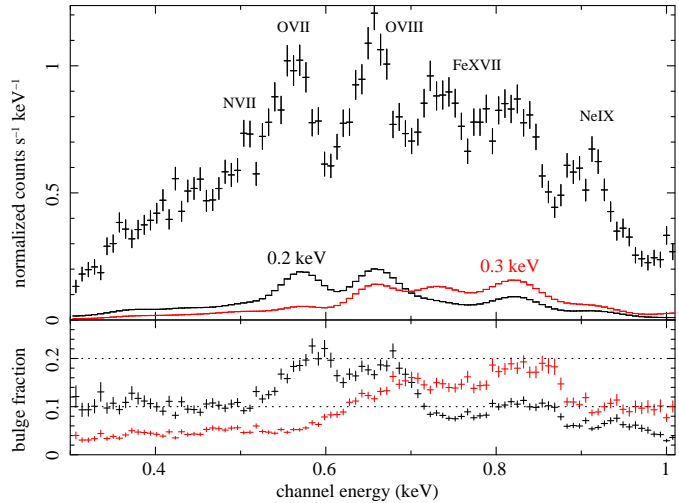


**Fig. 10.** Estimate of the contaminating flux from the Galactic bulge. The top panel shows the *Suzaku*/XIS1 spectrum of the NPS (points) plotted with the modeled Galactic X-ray bulge spectrum (solid lines) along this line of sight, assuming plasma with temperature 0.2 keV (black) and 0.3 keV (red) from the Almy et al. (2000) polytrope model. The bottom panel shows the fraction of the NPS spectrum attributable to the X-ray bulge model for each assumed temperature, with dotted lines marking 10% and 20%. The bulge emission accounts for up to 20% of the flux in the brightest lines and 10% or less in the remainder of the spectrum.

cts s<sup>-1</sup> keV<sup>-1</sup> is much greater than the scattered flux of 0.02 cts s<sup>-1</sup> keV<sup>-1</sup> estimated in Section 2.3.1. No other emission lines are expected at this energy. It is possible this excess is caused by a feature in the XIS1 response that has not been included in the calibration. In any case, the N VII line is seen in each of the FI spectra, which combined have an effective area 60% that of the BI at 0.5 keV. A fit performed on just the FI data yields similar results for N/O ratio, and we conclude the 0.54 keV excess has little effect on our results, including the nitrogen overabundance.

Previous studies using broad-band X-ray spectroscopy suggest a higher temperature of  $kT \approx 0.2$  keV for the GH component (e.g., Smith et al. 2007; Galeazzi et al. 2007). Indeed, a careful analysis of the *ROSAT* results suggests a two-temperature model for the so-called “transabsorption emission”, with  $kT_{\text{low}} \approx 0.1$  keV and  $kT_{\text{hi}} \approx 0.25$  keV (Kuntz & Snowden 2000). The NPS temperature derived by Willingale et al. (2003) is similar to that of the hot GH component, although they point out that the NPS emission is significantly brighter than the Kuntz & Snowden (2000) high-latitude emission within the observed band, and they ignore any contribution from the GH to the fitted NPS emission. A  $kT = 0.2\text{--}0.3$  keV component to the Galactic halo could produce a bright N VII emission line as well. Such material in CIE would also require enhanced N/O to explain the observed line ratios. In the few observations sensitive to N VII emission from diffuse Galactic gas, this is not found (McCammon et al. 2002; Fujimoto et al. 2007; Smith et al. 2007). As a result, the presence of a hotter GH component would dilute the considerably stronger NPS emission, and it would *increase* the derived

N/O ratio.

Additional contaminating flux may arise from Galactic bulge plasma, which has a temperature similar to that of the NPS (Snowden et al. 1997). Flux from the bulge would not be removed by subtracting the far-off-source NEP background, and could mimic emission from the NPS. The distribution of this material has been modeled by several authors (Snowden et al. 1997; Almy et al. 2000); to estimate the integrated flux along our sightline, we adopt the polytrope model of Almy et al. (2000). At a projected line-of-sight distance of 35° from the Galactic center, we expect a *ROSAT* 3/4 keV count rate of  $100 \times 10^{-6}$  cts s<sup>-1</sup> arcmin<sup>-2</sup> from the Galactic bulge plasma (Almy et al. 2000, Figure 6). Following the emission modeling of Almy et al. (2000), we produced a number of Raymond-Smith plasma models with this count rate (scaled to the observed XIS field of view) at a variety of temperatures in the expected range of 0.2–0.3 keV, folding through the XIS1 response. The results for 0.2 and 0.3 keV are presented in Figure 10, which shows the fraction of the observed XIS1 spectrum attributable to the modeled bulge. For 0.2 keV, the bulge accounts for up to 20% of the flux in the O VII and O VIII lines, and 10% or less of the flux elsewhere, including near the N VII line. For a 0.3 keV plasma, the bulge accounts for 20% of the flux in the O VIII and Fe lines, with less than 5% contamination at other energies. Intermediate temperatures contribute smaller fractions of the observed line flux.

A recent *Suzaku*/XIS observation towards a much brighter region of the X-ray-emitting bulge implies a somewhat lower contaminating flux. This region, towards

$(l, b) = (1.3^\circ, -14.5^\circ)$ , is about 4 times brighter in the *ROSAT* 3/4 keV map compared to the background region near the NPS. The XIS spectrum toward this region is 50% of the flux of our NPS spectrum in the oxygen emission lines (McCammon et al. in preparation). This implies a bulge contamination of about 10–15% of the total observed flux. The bulge spectrum also shows no N VII emission line. We conclude that while the Galactic bulge might produce a small fraction of the soft flux seen toward the NPS, it is unable to explain the enhanced N/O abundance ratio.

A single temperature for the NPS emission might be too simple, and the N/O ratio could be explained by multiple temperature components. Willingale et al. (2003) obtain an unusually high EM for the low- $kT$  GH component compared to other sightlines, as do we, and this is largely due to the very bright O VII line. It is impossible to produce O VII along with O VIII and the higher energy lines in the flux ratios observed with a single-temperature model. However, it is reasonable to believe that our line of sight probes multiple temperature components within the NPS, and that some of the O VII could be produced in cooler NPS plasma rather than the GH. We have investigated the effect of additional NPS temperature components on our fitting results. This does not change the quantitative fit, nor does it account for the flux of the N VII line without invoking a super-solar N/O ratio in the NPS plasma. We conclude that the enhanced nitrogen abundance observed toward the NPS is real and not a result of superposed, multi-temperature emission regions.

#### 4. Discussion

The NPS plasma conditions presented here are similar to the recent *XMM-Newton* results reported by Willingale et al. (2003) for three different pointings. Our temperature is slightly higher at  $kT = 0.29 \pm 0.01$  keV compared to 0.25–0.27 keV for *XMM-Newton* (90% confidence error bars). We obtain a similar intervening absorption column as Willingale et al. (2003), supporting the presence of a dense neutral sheet between the LHB and NPS bubbles. From the NPS emission parameters and a suitable model for the emission morphology, we can place constraints on the physical conditions of the plasma. We use the schematic model of Willingale et al. (2003), which consists of a bubble centered on  $l = 352^\circ$ ,  $b = +15^\circ$  at a distance of 210 pc with radius 140 pc. This structure is offset from and smaller than the Loop I bubble centered on the Sco-Cen association, and it is constructed to correspond to the bulk of the bright X-ray emission. Our pointing probes a path length of 157 pc through the NPS bubble. For an EM of  $0.10 \text{ pc cm}^{-6}$ , the electron density along the line of sight is  $n_e = 0.028 f^{-1/2} \text{ cm}^{-3}$ , where  $f$  is the volume filling factor and assuming uniform density within regions occupied by the hot gas. We also assume a fully ionized plasma with the best-fit abundances from our local background model, including a solar helium abundance. Given a best-fit temperature of 0.29 keV, the pressure from electrons and ions is  $P/k = 1.8 \times 10^5 f^{-1/2} \text{ cm}^{-3} \text{ K}$ . These

values are consistent with the *XMM* results. The total mass of hot gas in the NPS bubble is  $9.3 \times 10^3 f^{1/2} M_\odot$ , yielding a total thermal energy of  $1.2 \times 10^{52} f^{1/2} \text{ erg}$ . This is consistent with the energy output of a single supernova only if the filling factor of the gas is  $f \lesssim 0.01$ , much lower than expected for an evolved SNR. However, we note that most of the bubble has a much lower X-ray brightness than this field, therefore the density and energy derived here should be considered upper limits. The results are consistent with a bubble formed by one or more supernovae.

The abundances of O, Ne, Mg and Fe are consistent with previous results (Willingale et al. 2003) and are significantly subsolar, with  $\text{O}/\text{H} \approx 0.3$  solar compared to the Anders & Grevesse (1989) standard. Subsolar abundances are observed in other X-ray emission observations of the ISM (e.g., Miyata et al. 2007) as well as UV and X-ray absorption measurements (Meyer et al. 1997; Meyer et al. 1998; Takei et al. 2002; André et al. 2003; Yao & Wang 2006), and these fall in line with recent revisions in the standard solar abundance values (Asplund et al. 2005). Our derived O abundance is still about 50–60% of the revised solar value, though we have noted previously the difficulties of obtaining absolute metal abundances from X-ray emission data and stress that these values are not well-constrained. The ratios of Ne/O, Mg/O, and Fe/O are robust tracers of enrichment and are enhanced at 1.4–1.5 times the solar ratio.

The derived abundances of N and C are very different than those of other metals, and these are new results of this work. We observe an enhancement of N toward the NPS, with  $\text{N}/\text{H} = 1.3^{+0.5}_{-0.4}$  solar and  $\text{N}/\text{O} = 4.0^{+0.4}_{-0.5}$  solar. This is consistent with previous constraints: early X-ray observations suggest unusually strong N VI or N VII emission for the assumed NPS thermal model, although the limits are quite large (Inoue et al. 1980; Rocchia et al. 1984). The fields of view of these observations are also much larger than the *Suzaku*/XIS. Cawley (1998) used rocket-based CCD observations and obtained a best-fit N/O ratio of about 3, but with “unconstrained” error bars. Ours is the first clear detection of a N VII emission line toward the NPS.

We detect a C VI line in the XIS1 spectrum, but our best-fit local background model suggests it arises in the GH and LHB, not the NPS. This places an upper limit on the NPS abundance of  $\text{C}/\text{H} < 0.06$  solar and  $\text{C}/\text{O} < 0.2$  solar (limits are 90% confidence). The robustness of this results hinges on the nature of the GH component; at 0.1 keV, a solar abundance plasma must produce very strong C VI emission to also account for the bright O VII line. If there is a cooler NPS component with  $kT \approx 0.2$  keV, as discussed earlier, this could account for much of the O VII emission without filling in the C VI line completely, thus allowing some contribution from the hotter 0.3 keV NPS gas. The similar result for the local background and off-source background models suggests that the GH accounts for the full C VI and that the C/O deficit is real.

We can shed light on the N/O enhancement and possible C/O depletion by considering the mechanisms that

produce these metals. In the generally-accepted view of stellar metal enrichment, carbon and oxygen are produced primarily by helium shell burning in massive stars and released to the ISM through supernovae. Nitrogen, on the other hand, is produced largely by intermediate-mass ( $4\text{--}8 M_{\odot}$ ) stars and injected into the ISM via AGB winds (Henry et al. 2000). Carbon and oxygen are effectively converted to nitrogen during the CN branch of the CNO cycle, in which destruction of  $^{14}\text{N}$  is the limiting process ( $^{14}\text{N}(p,\gamma)^{15}\text{O}$ ; e.g., Clayton 1983). In AGB stars, this process occurs in the hydrogen-burning shell, with convection acting to cycle unprocessed envelope material through the CNO burning region and dredge-up returning this nitrogen-enriched material to the surface where it is released to the ISM in a strong stellar wind (Scalo et al. 1975; Iben & Renzini 1983). Evidence for large nitrogen enhancements and carbon deficiencies have been seen in AGB star envelopes (McSaveney et al. 2007). High mass evolved stars such as Wolf-Rayets and Luminous Blue Variables can also enrich their surroundings with nitrogen, although the effects of this appear to be small (Henry et al. 2000).

The large nitrogen overabundance observed in the NPS suggests enrichment by AGB activity of the X-ray emitting material, yet this is difficult to reconcile with the conventional view of the NPS origin. In the superbubble view, the combined effects of stellar winds and occasional supernovae from the Scorpius-Centaurus OB association have swept out a shell of hot material encompassed by the Loop I radio emission (de Geus 1992; Egger & Aschenbach 1995). The bright X-ray emission is produced by the most recent supernova shock wave (about  $10^5$  years old) heating the inner shell of the Loop I bubble, with an off-center progenitor star explaining the asymmetry (Egger & Aschenbach 1995). Photometric analysis of the Sco-Cen members (de Geus et al. 1989) and the measured expansion rate of the H I shell (Sofue et al. 1974; Heiles et al. 1980) constrain the age of the superbubble to be  $10^6\text{--}10^7$  yr, less than the  $10^8$  yr required for the first appearance of intermediate-mass AGB stars (Henry et al. 2000). It is therefore unlikely that the Sco-Cen association is responsible for the nitrogen enhancement in the reheated NPS plasma.

It is possible that the metal distribution of the NPS material was altered prior to formation of the Sco-Cen association and the Loop I superbubble. Observations of O I and N I absorption against stars using *HST* and *FUSE* suggest a systematic trend of lower nitrogen abundance and lower N/O ratio with increasing total hydrogen column density (Meyer et al. 1997; André et al. 2003; Knauth et al. 2003). Most notably, a recent reanalysis of these data shows a sharp drop in the ISM N/O ratio at a distance of 500 pc, with  $\text{N/O} \approx 1.7$  solar within this distance and near solar beyond it (Knauth et al. 2006). The NPS bubble as modeled lies fully within 500 pc radius, and while there is a discrepancy in the values of N/O, the trend of enhanced N/O ratio we infer is similar to that seen in the UV absorption observations.

Two possible mechanisms for this metallicity inhomogeneity

are suggested by Knauth et al. (2006). First, incomplete mixing of AGB wind and supernova products can alter the local abundance distribution for a short time. The observed N/O overabundance could result from enhanced AGB activity in the local Galaxy during the recent past. Second, localized infall of low-metallicity (perhaps primordial) gas could alter the abundance pattern, initially diluting all metals, but eventually producing a super-solar N/O ratio through enhanced intermediate-mass star production (Köppen & Hensler 2005). Further investigation is necessary to confirm the abundance inhomogeneity in different temperature phases and to identify its origin.

## 5. Summary

We have presented *Suzaku*/XIS observations of the North Polar Spur, observing the N VII emission line at 0.50 keV for the first time toward this sightline. Using two methods to account for the X-ray background, and assuming CIE, we determine the NPS plasma is best fit by a thermal APEC model with  $kT = 0.29 \pm 0.01$  keV and C, O, Ne, Mg, and Fe abundances of  $< 0.5$  solar. Nitrogen appears enhanced, with a best-fit N/O abundance ratio of  $4.0^{+0.4}_{-0.5}$  times the solar ratio. The temperature and total thermal energy of the gas suggest heating by multiple supernovae, consistent with previous models for the NPS and Loop I emission (Egger & Aschenbach 1995). The enhanced nitrogen abundance is best explained by enrichment from stellar material that has been processed by the CNO cycle, likely the result of enhanced AGB activity. Due to the time required to develop AGB stars, we conclude that this N/O enhancement cannot be caused by the Sco-Cen OB association, but may result from a previous enrichment episode in the solar neighborhood.

We owe a debt of gratitude to the entire *Suzaku* team for their support of the spacecraft and science operations. We thank Randall Smith, Norbert Nemes, and Eric Feigelson for valuable input, and thank the referee for useful comments that improved the manuscript. We also thank the ACE SWEPAM instrument team and the ACE Science Center for providing the ACE data. EDM acknowledges support from a Short-Term Postdoctoral Fellowship granted by the Japan Society for the Promotion of Science (JSPS). This work is financially supported by NASA grant NNG05GM92G and by a Grant-in-Aid for Scientific Research by the Ministry of Education, Culture, Sports, Science and Technology of Japan (16002004).

## References

- Almy, R. C., McCammon, D., Digel, S. W., Bronfman, L., & May, J. 2000, *ApJ*, 545, 290
- Anders, E. & Grevesse, N. 1989, *Geochim. Cosmochim. Acta*, 53, 197
- André, M. K. et al. 2003, *ApJ*, 591, 1000
- Arnaud, K. A. 1996, in *ASP Conf. Series*, Vol. 101, *Astronomical Data Analysis Software and Systems V*, ed.



- G. H. Jacoby & J. Barnes, 17
- Asplund, M., Grevesse, N., & Sauval, A. J. 2005, in ASP Conf. Series, Vol. 336, *Cosmic Abundances as Records of Stellar Evolution and Nucleosynthesis*, ed. T. G. Barnes, III & F. N. Bash, 25
- Bauer, F. E., Alexander, D. M., Brandt, W. N., Schneider, D. P., Treister, E., Hornschemeier, A. E., & Garmire, G. P. 2004, *AJ*, 128, 2048
- Berkhuijsen, E. M. 1971, *A&A*, 14, 359
- Berkhuijsen, E. M., Haslam, C. G. T., & Salter, C. J. 1971, *A&A*, 14, 252
- Bland-Hawthorn, J. & Cohen, M. 2003, *ApJ*, 582, 246
- Bunner, A. N., Coleman, P. L., Kraushaar, W. L., & McCammon, D. 1972, *ApJ*, 172, L67
- Cannon, A. & Pickering, E. 1918, *Annals of Harvard College Observatory*, 91
- Cawley, L. J. 1998, PhD thesis, The Pennsylvania State University
- Centurion, M. & Vladilo, G. 1991, *ApJ*, 372, 494
- Clayton, D. D. 1983, *Principles of stellar evolution and nucleosynthesis* (Chicago: University of Chicago Press)
- Cravens, T. E. 2000, *ApJ*, 532, L153
- Cruddace, R. G., Friedman, H., Fritz, G., & Shulman, S. 1976, *ApJ*, 207, 888
- Davelaar, J., Bleeker, J. A. M., & Deerenberg, A. J. M. 1980, *A&A*, 92, 231
- de Geus, E. J. 1992, *A&A*, 262, 258
- de Geus, E. J., de Zeeuw, P. T., & Lub, J. 1989, *A&A*, 216, 44
- De Luca, A. & Molendi, S. 2004, *A&A*, 419, 837
- Dickey, J. M. & Lockman, F. J. 1990, *ARA&A*, 28, 215
- Drake, S. A., Simon, T., & Linsky, J. L. 1989, *ApJS*, 71, 905
- Egger, R. J. 1995, in ASP Conf. Series, Vol. 80, *The Physics of the Interstellar Medium and Intergalactic Medium*, ed. A. Ferrara, C. F. McKee, C. Heiles, & P. R. Shapiro, 45
- Egger, R. J. & Aschenbach, B. 1995, *A&A*, 294, L25
- Fujimoto, R. et al. 2007, *PASJ*, 59, 133
- Galeazzi, M., Gupta, A., Covey, K., & Ursino, E. 2007, *ApJ*, 658, 1081
- Gelman, A. & Rubin, D. B. 1992, *Stat. Sci.*, 7, 457
- Hamaguchi, K. et al. 2007, *PASJ*, 59, 151
- Heiles, C., Chu, Y.-H., Troland, T. H., Reynolds, R. J., & Yegingil, I. 1980, *ApJ*, 242, 533
- Henry, R. B. C., Edmunds, M. G., & Köppen, J. 2000, *ApJ*, 541, 660
- Houk, N. & Swift, C. 2000, *Michigan Catalogue of HD stars*, Vol. 5
- Iben, Jr., I. & Renzini, A. 1983, *ARA&A*, 21, 271
- Inoue, H., Koyama, K., Matsuoka, M., Ohashi, T., Tanaka, Y., & Tsunemi, H. 1980, *ApJ*, 238, 886
- Ishisaki, Y. et al. 2007, *PASJ*, 59, 113
- Iwan, D. 1980, *ApJ*, 239, 316
- Knauth, D. C., Andersson, B.-G., McCandliss, S. R., & Moos, H. W. 2003, *ApJ*, 596, L51
- Knauth, D. C., Meyer, D. M., & Lauroesch, J. T. 2006, *ApJ*, 647, L115
- Köppen, J. & Hensler, G. 2005, *A&A*, 434, 531
- Koyama, K. et al. 2007, *PASJ*, 59, 23
- Kuntz, K. D. & Snowden, S. L. 2000, *ApJ*, 543, 195
- Mathewson, D. S. & Ford, V. L. 1970, *MmRAS*, 74, 139
- McCammon, D. et al. 2002, *ApJ*, 576, 188
- McSaveney, J. A., Wood, P. R., Scholz, M., Lattanzio, J. C., & Hinkle, K. H. 2007, *ArXiv e-prints*, 704
- Meyer, D. M., Cardelli, J. A., & Sofia, U. J. 1997, *ApJ*, 490, L103
- Meyer, D. M., Jura, M., & Cardelli, J. A. 1998, *ApJ*, 493, 222
- Miyata, E., Katsuda, S., Tsunemi, H., Hughes, J. P., Kokubun, M., & Porter, F. S. 2007, *PASJ*, 59, 163
- Picone, J. M., Hedin, A. E., Drob, D. P., & Aikin, A. C. 2002, *Journal of Geophysical Research (Space Physics)*, 107, 15
- Raines, J., Lepri, S. T., Zurbuchen, T. H., & et al. 2005, in *ESA SP-592: Solar Wind 11/SOHO 16, Connecting Sun and Heliosphere*, Vol. 16
- Roberts, T. P. & Warwick, R. S. 2001, in ASP Conf. Series, Vol. 234, *X-ray Astronomy 2000*, ed. R. Giacconi, S. Serio, & L. Stella, 569
- Rocchia, R. et al. 1984, *A&A*, 130, 53
- Scalo, J. M., Despain, K. H., & Ulrich, R. K. 1975, *ApJ*, 196, 805
- Schnopper, H. W. et al. *ApJ*, 253, 131
- Smith, R. K. et al. 2007, *PASJ*, 59, 141
- Smith, R. K., Brickhouse, N. S., Liedahl, D. A., & Raymond, J. C. 2001, *ApJ*, 556, L91
- Snowden, S. L. 1998, *ApJS*, 117, 233
- Snowden, S. L., Cox, D. P., McCammon, D., & Sanders, W. T. 1990, *ApJ*, 354, 211
- Snowden, S. L. et al. 1997, *ApJ*, 485, 125
- Snowden, S. L. & Freyberg, M. J. 1993, *ApJ*, 404, 403
- Sofue, Y. 1977, *A&A*, 60, 327
- Sofue, Y. 1984, *PASJ*, 36, 539
- Sofue, Y. 1994, *ApJ*, 431, L91
- Sofue, Y. 2000, *ApJ*, 540, 224
- Sofue, Y. 2003, *PASJ*, 55, 445
- Sofue, Y., Hamajima, K., & Fujimoto, M. 1974, *PASJ*, 26, 399
- Stone, E. C., Frandsen, A. M., Mewaldt, R. A., Christian, E. R., Margolies, D., Ormes, J. F., & Snow, F. 1998, *Space Science Reviews*, 86, 1
- Takei, Y., Fujimoto, R., Mitsuda, K., & Onaka, T. 2002, *ApJ*, 581, 307
- Tawa, N. et al. 2007, *PASJ*, submitted
- Verkhodanov, O. V., Kopylov, A. I., Pariiskii, Y. N., Soboleva, N. S., Temirova, A. V., & Zhelenkova, O. P. 2002, *Astronomy Reports*, 46, 531
- Voges, W. et al. 1999, *A&A*, 349, 389
- Willingale, R., Hands, A. D. P., Warwick, R. S., Snowden, S. L., & Burrows, D. N. 2003, *MNRAS*, 343, 995
- Yao, Y. & Wang, Q. D. 2006, *ApJ*, 641, 930